



Available online at [www.sciencedirect.com](http://www.sciencedirect.com)

**SciVerse ScienceDirect**

Advances in Space Research 52 (2013) 496–504

**ADVANCES IN  
SPACE  
RESEARCH**  
(*a COSPAR publication*)  
[www.elsevier.com/locate/asr](http://www.elsevier.com/locate/asr)

# Charge exchange interactions on near-Earth proton radiation for orbit perturbation of high area-to-mass ratio objects

Lake A. Singh\*, Mitchell L.R. Walker

*Aerospace Engineering, Georgia Institute of Technology, 270 First Dr. NW, Atlanta, GA 30332, USA*

Received 4 January 2013; received in revised form 18 March 2013; accepted 26 March 2013

Available online 6 April 2013

---

## Abstract

This novel concept expels neutral gas in the presence of geomagnetically-trapped protons in near-Earth orbit. The expelled neutral gas acts to induce charge exchange collisions with the geomagnetically-trapped protons and induce drag on objects which pass through it. The charge exchange collisions between the neutral gas and the geomagnetically-trapped protons create neutrals with similar kinetic energy that are not confined by the geomagnetic field. The charge exchange neutrals are able to collide with orbital objects and perturb their orbits. The delta- $v$  applied by the charge exchange neutral flux is greatest on high area-to-mass objects. Numerical simulation shows charge exchange neutral impacts produce a delta- $v$  on objects on the order of  $3.8 \times 10^{-11}$  m/s at a distance of 1 km from the center of the expelled gas in a 1,000 km orbit. The impulse imparted by charge exchange neutral impacts is at least six orders of magnitude smaller than that provided by the induced drag caused by gas expulsion. The localized drag increase can force a majority of small objects into the orbit of the expelled gas cloud, even if that orbit is retrograde to the initial orbit of the objects. This new technique can be applied to the remediation of space debris.

© 2013 COSPAR. Published by Elsevier Ltd. All rights reserved.

**Keywords:** Charge exchange; Proton radiation; Van Allen belts; Space debris; Drag; Area-to-mass ratio

---

## 1. Introduction

One challenge in space engineering is the orbit manipulation of objects of interest which are uncontrolled. The only demonstrated method of orbit manipulation of an uncontrolled object is direct interaction and capture as was done with the capture and return of the Long Duration Exposure Facility (LDEF) by the Shuttle *Columbia* in 1990. The capture method is a technically feasible option for large, trackable objects; but there is still no way to manipulate smaller, untrackable objects. For large populations of untrackable objects, the energy costs associated with individually interacting with each object becomes very high.

One specific type of problem which fits this description and directly confronts the space community is space debris. In particular, the population of debris smaller than 1 cm in diameter numbers in the trillions (Belk et al., 1997). Debris of this physical scale in low Earth orbit (LEO) can have wide-ranging lifetimes which can extend from a few years to thousands of years depending on factors including the orbit altitude and debris area-to-mass ( $A/m$ ) ratio (Gibbons, 1995; Anselmo and Pardini, 2009; Pardini and Anselmo, 2011). Because of current limitations in tracking debris of this physical scale and its long lifetime, space debris of this physical scale presents a growing long term danger to operational spacecraft.

Space debris objects vary greatly in size, geometry and material. Large objects such as defunct satellites and expended rocket stages make up the largest types of space debris, and may be several meters in diameter. Debris in this size range is detected and tracked from the ground and consequently avoided by active spacecraft. Spacecraft

\* Corresponding author. Tel.: +1 404 463 7589.

E-mail addresses: [lake1@gatech.edu](mailto:lake1@gatech.edu) (L.A. Singh), [mitchell.walker@ae.gatech.edu](mailto:mitchell.walker@ae.gatech.edu) (M.L.R. Walker).

and rocket stages sometimes break apart and form a larger number of smaller, harder to detect debris (Patera and Ailor, 1998). Many of the objects in this size range are not tracked or catalogued and consequently pose the greatest risk to active spacecraft (Mehrholz et al., 2002). At the smallest diameters, objects such as paint chips, explosive bolt fragments, micrometeoroids, and thermal insulation fragments form an innumerable quantity of small scale debris which is impossible to detect and track from the ground. While shielding can effectively stop penetration from debris at this scale, it still poses a constant risk to sensitive exposed areas on spacecraft such as lenses, antennae, windows, and solar panels (Christiansen and Kerr, 2001; Bernhard et al., 1995).

For the largest space debris, active debris removal may become a necessity to permit the continued exploitation of highly populated orbits (Liou et al., 2010). The necessity for removal might ultimately extend to small objects as well as the debris environment develops from future events. An effective small debris removal mechanism interacts with multiple objects simultaneously and leverages energy sources available on-orbit.

The manipulation of high  $A/m$  ratio objects is a topic of current scientific interest not only for space debris, but also because of the current trends towards miniaturization in spacecraft design and non-traditional propulsion. Consideration of many environmental sources of acceleration effective particularly for high  $A/m$  objects exist in literature (Atchison and Peck, 2011), mainly involving solar radiation pressure (Colombo et al., 2013; Kawaguchi et al., 2009) or atmospheric drag (Anselmo and Pardini, 2009).

This work presents the novel concept of utilizing the near-Earth proton radiation environment as a source of energy and momentum for remotely and simultaneously manipulating multiple high  $A/m$  ratio objects, with particular attention paid toward its application for the reduction of space debris lifetime. This is an unconsidered environmental source for acceleration of high  $A/m$  ratio objects in literature.

### 1.1. Proton radiation belt

The Van Allen belts are regions in the Earth's geomagnetic field that magnetically confine charged protons from the solar wind and cosmic sources (Van Allen et al., 1961). Earth's geomagnetic field is approximately a dipole field which has converging field lines near the poles (Bau-mjohann and Treumann, 1997). The convergence of field lines acts as a magnetic mirror which confines the charged particles along the field lines. Particles' energies dictate how far along the field lines they move towards the poles before reflecting back towards the opposite pole. This mirror confinement effect leads to the structure of the Van Allen belts.

Earth's geomagnetic field is not a perfect dipole. There are perturbations of the geomagnetic field from external

sources. Predominant among these external sources is solar activity, which has stripped away the belts in the past (Baker et al., 2004). Variation in the geomagnetic field from a perfect dipole also leads to a region of high radiation at low altitude known as the South Atlantic Anomaly (SAA) (Vernov et al., 1967). While the radiation belts typically start outside of low Earth orbit (LEO), the SAA penetrates down below an altitude of 250 km and leads to documented effects on both satellites and humans (Vernov et al., 1967; McCormack, 1988). For the purposes of the analysis presented in this paper, variations as a result of solar activity and geomagnetic asymmetry are neglected.

## 2. Approach

This work proposes the release of neutral gas clouds into the near-Earth environment. Releasing the gas cloud produces a temporary increase in the neutral number density near the release point of the gas cloud. The increased neutral number density produces two distinct effects. The first effect is an increase in drag on objects as they pass through the expanding gas cloud. An increase in drag means increased momentum transfer from the objects which ultimately leads to a modification of the orbit parameters of the objects towards higher eccentricity and lower semi-major axis.

At the same time, an increase in neutral number density leads to an increase in charge exchange (CEX) collisions with geomagnetically-trapped protons passing through the expanding gas cloud. The CEX collisions begin with confined geomagnetically-trapped protons and unconfined low energy neutrals, and result in unconfined energetic neutralized protons and confined low energy ions. The basic reaction is given in Eq. (1). Unconfined energetic neutralized protons travel along their post-collision trajectories until they collide with other particles, where they transport momentum. An increase in drag and CEX collisions caused by an increase in neutral number density are independent and additive.



The proposed approach presents some positive features for remediation of debris smaller than 1 cm in diameter. Releasing neutral gas clouds into orbit bands does not produce any additional contribution to the debris population. A gas cloud released into space very rapidly dissipates down to the background density in tens of seconds, depending on the background density and the initial gas cloud conditions at release. The proposed approach makes use of energy available on-orbit from the trapped proton radiation field to reduce the ground-to-space energy cost. By controlling the location and timing of release, the proposed approach can avoid interference with normal space operations. Since the gas cloud has a short lifetime, critical regions can be cleared out while operational assets are present.

### 3. Simulation of effect

#### 3.1. CEX effect

Numerical simulation of the proposed concept provides insight into its effectiveness at remotely applying impulse. Analysis begins at the determination of the rate of CEX collisions in the neutral gas caused by the flux of geomagnetically-trapped protons. For analysis, the gas cloud is assumed to be composed entirely of nitrogen ( $N_2$ ) which is available in situ (Hedin, 1988). Eq. (2) is an expression for the bimolecular collision rate from kinetic theory adapted to this purpose. The collision rate of  $N_2$  and protons resulting in CEX  $z$  is a function of the number density of protons  $n_{p^+}$ , the number density of nitrogen molecules  $n_{N_2}$ , the cross section for CEX collision  $\sigma$ , and the relative velocity between the two  $\bar{g}$ . These values are in turn functions of the energy of the protons  $E$ , the density of the neutral gas  $\rho$ , the total number of neutral particles  $N$ , and the position in the geomagnetic field (given by coordinates  $L$  and  $B$ ).

$$\begin{aligned} Z_{N_2,p^+}(E, L, B, \rho(r, t), N_{N_2}) \\ = n_{p^+}(E, L, B) n_{N_2}(\rho(r, t), N_{N_2}) \rho(E) \bar{g}(E) \end{aligned} \quad (2)$$

The first value of interest, the number density of protons, comes from the AP-8 MIN model produced by NASA (Sawyer and Vette, 1976). It assumes a perfect dipole field at a solar minimum which neglects latitudinal position variations in the radiation field. The solar minimum model is selected because it provides the highest flux values (Stassinopoulos and Raymond, 1988). The model interpolates smoothed data sets to provide the flux of geomagnetically-trapped protons in space around the Earth as a function of modified McIlwain  $L$ -shell coordinates and the desired energy range (McIlwain, 1961). The  $L$ -shell coordinate system is an efficient way to map a dipole field. The first coordinate,  $L$  denotes a field line and is given by:

$$L = \frac{r_{eq}}{R_E} \quad (3)$$

where  $r_{eq}$  is the magnetic equatorial distance of the field line from the center of the Earth and  $R_E$  is the radius of the Earth. The value of  $r_{eq}$  for a given point in space is:

$$r_{eq} = \frac{r}{\cos^2 \lambda} \quad (4)$$

where  $r$  is the distance of the point from the center of the Earth, and  $\lambda$  is the magnetic latitude. The magnetic latitude is different from the geographic latitude in that it denotes latitude from the magnetic polar axis rather than the geographical polar axis. The two are offset from one another depending on geographic location. The second coordinate in the McIlwain  $L$ -shell system is  $B$ , which is the strength of the dipole field.  $B$  is expressed as:

$$B(\lambda, L) = \frac{B_E}{L^3} \frac{(1 + 3 \sin^2 \lambda)^{\frac{1}{2}}}{\cos^6 \lambda} \quad (5)$$

with  $B_E$ , the dipole strength at the magnetic equatorial surface of the Earth. The AP-8 MIN model takes in a modified parameter,  $B/B_0$  which is a ratio of the dipole strength at the point of interest and the dipole strength at the magnetic equatorial intersection of the field line. Taking the magnetic latitude to be zero and dividing through yields a value of  $B/B_0$  which is a function of  $\lambda$  only:

$$\frac{B}{B_0}(\lambda) = \frac{(1 + 3 \sin^2 \lambda)^{\frac{1}{2}}}{\cos^6 \lambda} \quad (6)$$

It should be noted that the resulting equations for mapping  $L$  and  $B/B_0$  (from now on referred to simply as  $B$ ) are independent of magnetic longitude. This result means anomalies or asymmetries in the actual field such as the SAA are lost in the approximation of the model. Despite this limitation, the AP-8 MIN model provides an estimate within a factor of two of proton fluxes (Sawyer and Vette, 1976).

Fluxes ( $n''_{p^+}$ ) provided by the AP-8 MIN model are converted into number densities by dividing by the proton velocity, as shown in Eq. (7). The proton velocity is approximately the same as the relative velocity between the neutral gas and the proton velocity because the proton velocity is much greater than the neutral gas thermal velocity. As such, the relative velocity is determined only from the energy of the protons and their mass  $m_p$ , as shown in Eq. (8).

$$n_{p^+}(E, L, B) = \frac{n''_{p^+}(E, L, B)}{g(E)} \quad (7)$$

$$\bar{g}(E) \approx \sqrt{\frac{2E}{m_p}} \quad (8)$$

The neutral gas number density,  $n_{N_2}$  is a function of the density of the neutral gas which is determined by the initial conditions on the gas cloud and the total number of neutral gas particles. The initial configuration selected is that of a uniform sphere which expands into a vacuum. From (Mommud, 1960), the density of the initially uniform, expanding spherical neutral gas cloud as a function of time and distance from the center of the cloud is:

$$\begin{aligned} \rho(d, t) = \frac{1}{2} \left\{ \text{erf} \left[ (d+a)\beta^{\frac{1}{2}}t^{-1} \right] - \text{erf} \left[ (d-a)\beta^{\frac{1}{2}}t^{-1} \right] \right\} \\ + \frac{1}{2} t (d^2 \beta \pi)^{-\frac{1}{2}} \left\{ \exp \left[ -\frac{(a+d)^2 \beta}{t^2} \right] - \exp \left[ -\frac{(a-d)^2 \beta}{t^2} \right] \right\} \end{aligned} \quad (9)$$

where  $\rho_0$  is the initial uniform density inside the cloud at  $t = 0$ , and  $a$  is the initial radius of the cloud at  $t = 0$ .  $\beta$  is the quantity  $m_{N_2}/2kT$ , where  $k$  is the Boltzmann constant and  $T$  is temperature. Eq. (9) is an analytic solution found by remapping a thermodynamic solution which is derived in (Carslaw and Jaeger, 1959). The initial density and  $\beta$  result from the selection of initial temperature and pressure via the ideal gas law. The time and space varying neutral gas density lead to the neutral gas number density by dividing by the molecular mass of the neutral gas,  $m_{N_2}$ . The only

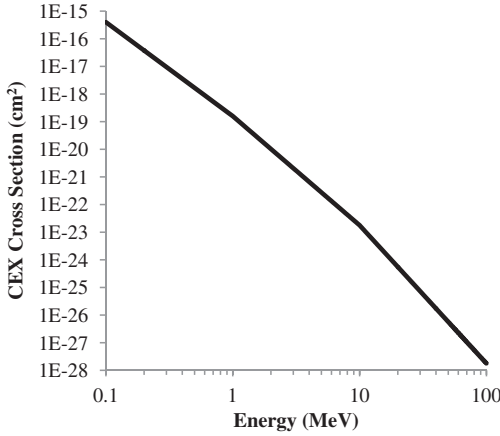


Fig. 1. Nitrogen-proton CEX cross section data as a function of energy used in this work. The curve presented is a power-law approximation of data provided in Mapleton (1965) and Welsh et al. (1967).

remaining quantity in Eq. (2), the cross section for CEX collision, is an approximation of the experimental and theoretical data reported graphically in Welsh et al. (1967) and Mapleton (1965). Three power law functions over each of the three energy decades of interest approximates their results for this work. Fig. 1 shows the CEX cross-section data used in this work over the energy range of interest.

Integration of the CEX collision rate in space and time yields the total number of CEX collisions as a function of proton energy and the total neutral gas population. This value is calculated as shown in Eq. (10), and corresponds to the total number of energetic neutralized protons produced by the emission of the neutral gas cloud in the radiation field. By assuming a spherically-symmetric distribution of the energetic neutralized protons from a point source at the center of the gas cloud, Eq. (11) calculates a surface density of energetic neutralized protons at a distance  $d$  from the center of the cloud. The surface density represents the time integrated flux of  $N_{CEX}$  from the center of the neutral gas cloud. Only selecting distances  $d$  which are much greater than the radius over which CEX collisions are simulated justifies the point source assumption.

$$N_{CEX}(E, L, N_{N_2}) = \int \int z_{N_2, p^+}(E, L, B, \rho(r, t), N_{N_2}) dV dt \quad (10)$$

$$n''(N_{CEX}(E, L, B, N_{N_2}), d) = \frac{N_{CEX}(E, L, B, N_{N_2})}{4\pi d^2} \quad (11)$$

Integration of the product of the surface density of energetic neutralized protons, the proton mass, and the energetic neutralized proton velocity over all energies as shown in Eq. (12) yields an effective impulse per unit area  $\Delta p$  at a distance  $d$  from the center of the gas cloud. This calculation relies on two major assumptions. The energetic neutralized protons are assumed to not pass through remote objects of interest upon collision, and all collisions are assumed to be perfectly inelastic.

$$\Delta p''(N_{N_2}, L, B, d) = \int n''(N_{CEX}(E, L, B, N_{N_2}), d) m_{p^+} \bar{g}(E) dE \quad (12)$$

The validity of these assumptions relies on the thickness of remote objects being large enough to prevent penetration by the energetic neutralized protons. If the remote objects are too thin, the majority of neutral particles will penetrate through them without exchanging most of their momentum. Rutherford elastic scattering provides insight into the minimum thickness for which the inelastic assumption is still valid. The mean free path,  $\lambda$  through a solid of interest is given simply by:

$$\lambda = \frac{1}{n\sigma} \quad (13)$$

where  $n$  is the number density of the solid and  $\sigma$  is the cross section for scattering. Aluminum is selected as a representative solid to provide a simple estimate of the mean free path for the energetic neutralized protons, and determines the number density. The cross section on the other hand is given by Eq. (14) for azimuthally-symmetric scattering (Griffiths, 2005). The differential cross section depends on the charge of each species present  $q_i$ , the vacuum permittivity  $\epsilon_0$ , the energy  $E$ , and the scattering angle  $\theta$ . The scattering angle itself is a function of the impact parameter  $b$ , which is the closest approach between nuclei and relates to the scattering angle by Eq. (15). Assumption of a maximum impact parameter determines a minimum scattering angle over which to integrate the differential cross section. Assuming a maximum impact parameter of 0.1 nm and an energy of 1 MeV, the minimum scattering angle of interest is 0.187 m rad, which leads to a total cross section of  $6.28 \times 10^{-20} \text{ m}^2$  and a mean free path of  $2.66 \times 10^{-10} \text{ m}$ . By assuming such a large impact parameter small angle scattering is adequately accounted for. Thus, if the thickness of the aluminum exceeds the product of the ratio of 90° and the minimum scattering angle and this mean free path then the inelastic assumption made for Eq. (12) is justified. For aluminum, this corresponds to a sheet thickness of 3 μm, or an  $A/m$  ratio of approximately 140  $\text{m}^2/\text{kg}$ . This is 40% higher than the maximum  $A/m$  ratio of 100  $\text{m}^2/\text{kg}$  considered here.

$$d\sigma = \left[ \frac{q_1 q_2}{16\pi\epsilon_0 E \sin^2(\frac{\theta}{2})} \right]^2 2\pi \sin\theta d\theta \quad (14)$$

$$B = \frac{q_1 q_2}{8\pi\epsilon_0 E} \cot\left(\frac{\theta}{2}\right) \quad (15)$$

Finally, using the effective impulse per unit area and given an  $A/m$  ratio, the average  $\Delta v$  on a remote object can be calculated using Eq. (16). This equation shows that the  $\Delta v$  on a remote object from utilization of the proposed concept is a function of its  $A/m$  ratio, the amount of neutral gas deployed, geomagnetic location, and the distance from the neutral gas cloud.

$$\Delta v \left( d, N_{N_2}, L, B, \frac{A}{m} \right) = \Delta p''(N_{N_2}, L, B, d) \frac{A}{m} \quad (16)$$

Inputting analytically solvable expressions for the relative velocity, cross section, and gas cloud density as functions of time, distance from the gas cloud center, and energy produce results from the program which can be compared to the analytical solutions to verify the accuracy of the program. Using a sufficiently fine solution grid in the time, distance from the gas cloud center, and energy space allows the program to calculate an answer to within one percent for analytical expressions which scale similarly to the actual data.

### 3.2. Drag effect

Analysis of the average effect of drag from the expanding gas cloud on the debris field provides a standard by which to quantify the effectiveness of the CEX technique. The analysis performed is a Monte Carlo simulation of the expanding gas cloud in the presence of a flux of debris as predicted by NASA's ORDEM 2000 code (Liou et al., 2002). The simulation consists of three components: the time and space evolving density function given by Eq. (9), the particles inputted into the system, and the simulation of their motion through the density field. This analysis is not meant to precisely predict the effect of the cloud on the debris field, but rather to provide a first-order estimate of its potential for space debris remediation. As such, a number of assumptions are employed to simplify the analysis.

The domain of the simulation consists of a cube of space 14 km on a side spanning 25 s of time, beginning with the initial release of the gas cloud and located at an altitude of 1000 km. These bounds are selected because the density drops to small values beyond this domain ( $\sim 10^{-9} \text{ kg/m}^3$ ) which do not significantly affect simulated particles. A 5000 kg nitrogen gas bubble, with initial pressure and temperature of 10 MPa and 300 K expands from the center of the cube starting at time  $t = 0$  using Eq. (9). Fig. 2 shows the profile of the gas density field over  $r/a$  for differing val-

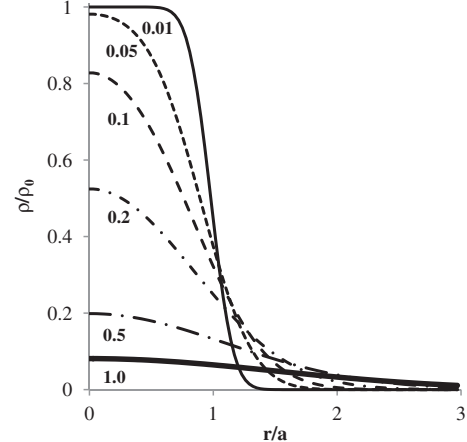


Fig. 2. Plots of  $\rho(r/a, t)/\rho_0$  as calculated by the drag simulation for differing values of  $t^2(4\beta a^2)^{-1}$  annotated in the figure. The plot matches that shown in Molmud (1960).

ues of  $t^2(4\beta a^2)^{-1}$  (a similarity parameter for Eq. (9)). The results match those shown in Molmud (1960).

The simulation generates and inserts debris objects into the simulation volume at a rate which matches debris flux values obtained from ORDEM 2000. For this work, ORDEM 2000 debris flux and relative velocity values at 1000 km altitude for three different orbits ca. 2007 provide the input debris conditions into the simulation. The three orbits include a 1000 km altitude equatorial circular orbit, a 1000 × 200 km altitude equatorial elliptical orbit, and a 1000 × 200 km altitude retrograde equatorial elliptical orbit. Table 1 provides the values obtained by ORDEM 2000 for each case and used in the simulation. Objects inserted into the simulation have diameter equal to one of the four values given in Table 1 and have velocity equal to the corresponding average relative velocity. Assuming the objects all have diameter equal to the minimum possible diameter for the inequality makes the estimate from this simulation a conservative one. Area equal to four sides of the simulation cube multiplies the obtained flux values to obtain the rate at which objects of each diameter should be input into the simulation. The area for the faces of the

Table 1  
Debris flux and relative velocity values obtained from ORDEM 2000 and used in the simulation.

Diameter	>10 μm	>100 μm	>1 mm	>1 cm
<i>Case 1: 1000 km altitude equatorial circular orbit</i>				
Debris flux ( $\text{m}^2\text{-yr}^{-1}$ )	2690	145	0.225	$3.58 \times 10^{-5}$
Relative velocity (km/s)	4.89	5.54	4.47	8.81
<i>Case 2: 1000 × 200 km altitude equatorial elliptical orbit</i>				
Debris flux ( $\text{m}^2\text{-yr}^{-1}$ )	2710	146	0.226	$3.59 \times 10^{-5}$
Relative velocity (km/s)	4.94	5.55	4.53	8.66
<i>Case 3: 1000 × 200 km altitude retrograde equatorial elliptical orbit</i>				
Debris flux ( $\text{m}^2\text{-yr}^{-1}$ )	8440	385	0.788	$4.73 \times 10^{-5}$
Relative velocity (km/s)	15.3	14.7	15.6	11.6

simulation cube normal to the nadir are not accounted for because objects fluxing through those faces will have very high eccentricity and thus be short lived.

Since the gas expansion is spherically symmetric all objects can be introduced into the simulation cube on the same face with velocity in the direction of the opposite face on the simulation volume without loss of fidelity. The time at which objects are put into the simulation and the position on the input face are randomly determined. The  $A/m$  ratio in  $\text{m}^2/\text{kg}$  for input objects is given by the distribution:

$$\frac{A}{m} = 10^G \quad (17)$$

where  $G$  is a standard normally distributed random value with mean equal to zero and standard deviation equal to 1. The distribution is cut off at  $100 \text{ m}^2/\text{kg}$  on the high end and the  $A/m$  ratio for an aluminum sphere of the specified minimum diameter at the low end. The choice of distribution is arbitrary, but manages to represent objects from the entire  $A/m$  ratio range of interest. Fig. 3 shows the resulting distribution of  $A/m$  ratio for the different minimum diameters given in Table 1.

The simulation propagates the velocity and position of simulated debris objects as they pass from one side of the simulation cube to the other. Eq. (18) provides the equa-

tion of motion used for the propagation, where  $C_D$  is the drag coefficient and  $x$  is the position of the object. For simplicity, a drag coefficient of 2.2 is assumed for all particles at all velocities. This is a common assumption for first order analyses of drag (Cook, 1965; Zhou et al., 2009). Drag coefficient values could vary from less than one to greater than three, depending on the actual geometry of the object and the flow conditions (Vallado and Finkelman, 2008). Because details about the geometry are beyond the fidelity of this simulation it instead implements a value between the two extremes. The initial velocity for Eq. (18) is also taken to be equal to the average relative velocity as provided in Table 1 rather than the relative velocity between the expanding gas and the object. The expanding gas has velocity roughly equal to the thermal velocity in the radial direction from the center of the simulation volume and is roughly one tenth the average relative velocity of the particles. Thus, its exclusion introduces a roughly 21% error in the calculation. Results from the simulation are averaged over a large number of statistically independent runs to determine the average effect of the gas cloud on the nearby debris field.

$$\ddot{x} = -\frac{C_D}{2} \rho(r, t) \frac{A}{m} \dot{x}^2 \quad (18)$$

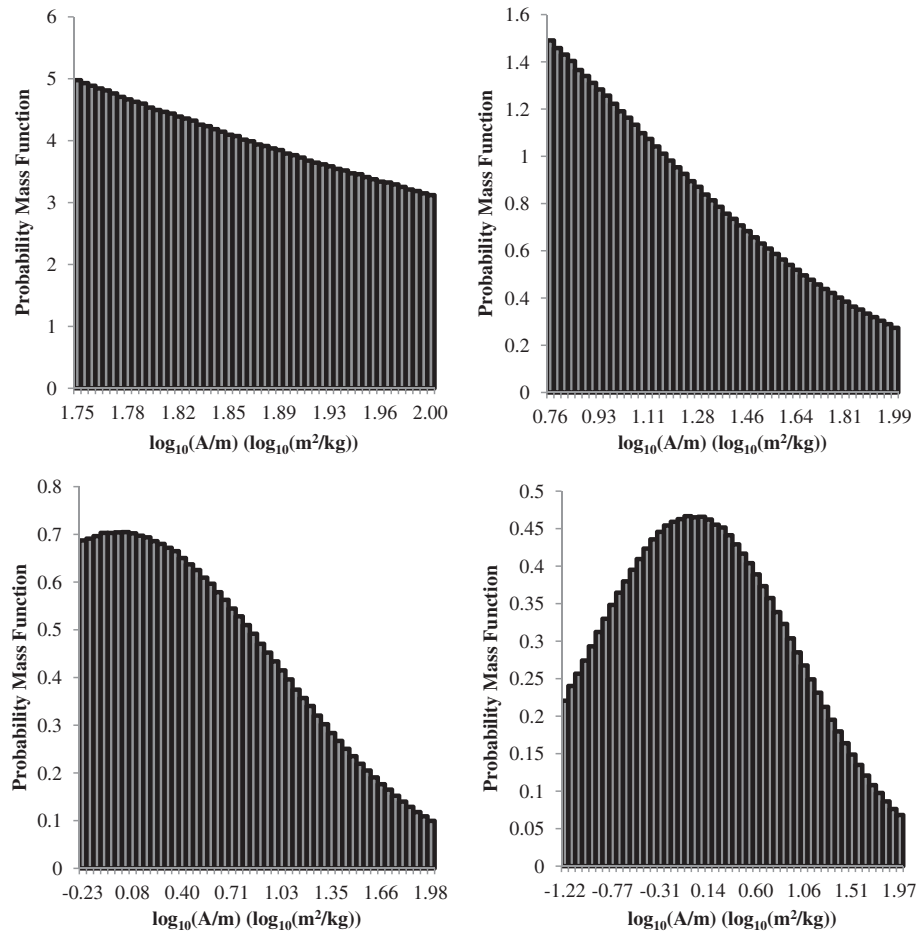


Fig. 3. Histograms of  $\log_{10}(A/m)$  for different diameters. Top left: 10  $\mu\text{m}$ . Top right: 100  $\mu\text{m}$ . Bottom left: 1 mm. Bottom right: 1 cm.

#### 4. Results and discussion

The equations laid out in the previous section are employed in the numerical simulation of the CEX concept. Simulations are performed at two geomagnetic coordinates: the first being those coordinates which correspond to a 1000 km orbital altitude at the magnetic equator ( $L = 1.15$ ,  $B/B_0 = 1$ ), and the second at  $L = 3.2$  and  $B/B_0 = 1$  which corresponds to the region of highest proton flux and an orbital altitude of 14,031 km. The distance from the initial neutral gas cloud center, total gas cloud mass, and  $A/m$  ratio of remote objects are all varied to confirm the validity of the numerical methods applied and relationships predicted by the equations. Namely, the equations indicate that the  $\Delta v$  should vary linearly with the  $A/m$  ratio and total neutral gas mass, and as the inverse square of the distance from the center of the initial cloud.

The results indicated in Figs. 4–7 confirm these relationships at both 1000 and 14,031 km. In Fig. 4 the distance is varied on the ordinate while the initial neutral gas cloud mass is held constant at 5000 kg and the  $A/m$  ratio at 50 m<sup>2</sup>/kg. The predicted inverse square relationship is observed in the results. This relationship is in line with the space variation in density from an expanding gas cloud, but ultimately arises from the point source assumption made by the model. In Fig. 5 the  $A/m$  ratio is varied on the primary ordinate while neutral gas mass is varied on the secondary ordinate for a constant distance of 1 km. For the varying neutral gas mass data the  $A/m$  ratio is held constant at 50 m<sup>2</sup>/kg while for the varying  $A/m$  ratio data the neutral gas mass is held constant at 5000 kg. In the case of varying  $A/m$  ratio the  $\Delta v$  varies linearly with increasing  $A/m$  ratio because increasing the ratio decreases the affected mass for the same quantity of impulse. We must however be careful not to extrapolate this trend too far

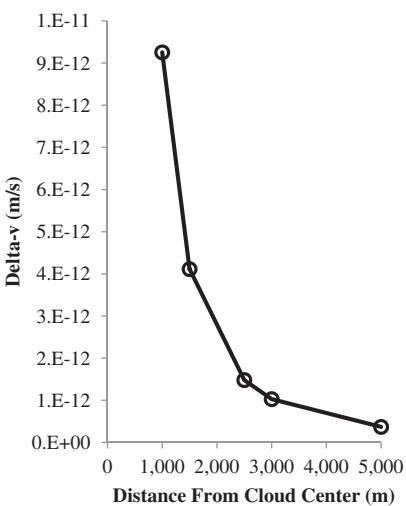


Fig. 4. Simulation results for  $\Delta v$  on an object with area-to-mass ratio of 50 m<sup>2</sup>/kg and initial gas cloud mass of 5000 kg deployed at 1000 km altitude. The distance of the object is varied, with simulation points given by circular markers.

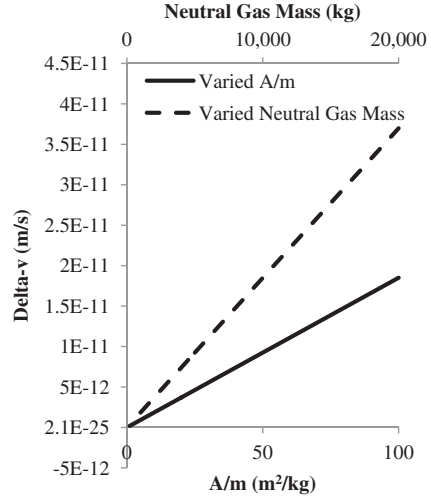


Fig. 5. Simulation results for  $\Delta v$  on a remote object. The dashed line represents varying initial gas cloud mass at constant  $A/m$  equal to 50 m<sup>2</sup>/kg. The solid line represents varying area-to-mass ratio at constant neutral gas mass equal to 1000 kg. Both data sets have a constant distance from the gas cloud center of 1 km and gas cloud altitude of 1000 km.

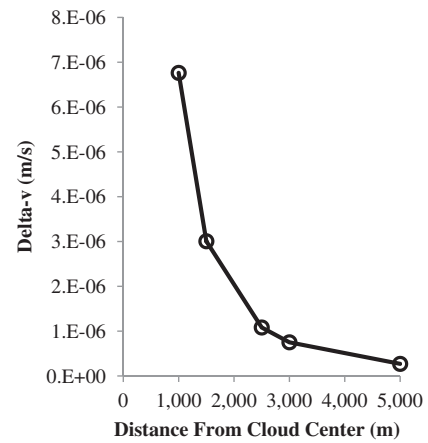


Fig. 6. Simulation results for  $\Delta v$  on an object with area-to-mass ratio of 50 m<sup>2</sup>/kg and initial gas cloud mass of 5000 kg deployed at 14,031 km altitude. The distance of the object is varied, with simulation points given by circular markers.

so as not to risk leaving the range where the inelastic assumption is justified.

In the case of the varying neutral gas cloud mass, the  $\Delta v$  again increases linearly with increasing mass. As the mass is increased, more neutrals are present in the system and thus the CEX collision rate rises. However, the presence of increased gas mass also increases the effectiveness of the gas itself at affecting remote objects. In each case the predicted scaling of  $\Delta v$  is seen, which further validates the numerical method. Of particular note in both of these datasets is the range of  $\Delta v$  attained at a cloud altitude of 1000 km. The highest  $\Delta v$  attained within the simulations performed at this altitude is only  $3.7 \times 10^{-11}$  m/s for a distance of 1 km, gas mass of 20,000 kg, and  $A/m$  ratio of 50 m<sup>2</sup>/kg. At a 1000 km circular orbit, a Hohmann transfer

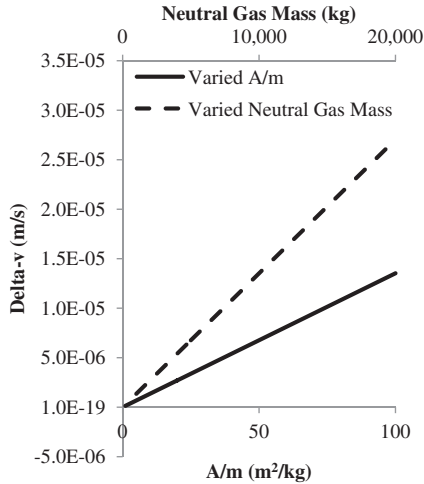


Fig. 7. Simulation results for  $\Delta v$  on a remote object. The dashed line represents varying initial gas cloud mass at constant  $A/m$  equal to  $50 \text{ m}^2/\text{kg}$ . The solid line represents varying area-to-mass ratio at constant neutral gas mass equal to 1000 kg. Both data sets have a constant distance from the gas cloud center of 1 km and gas cloud altitude of 14,031 km.

with this  $\Delta v$  changes the apogee by 0.07 nm. These results indicate that deployment of a gas cloud at an altitude of 1000 km does not apply sufficient impulse through CEX to meaningfully change the orbit of objects due to the limited density of geomagnetically-trapped protons in that region of the geomagnetic field.

The effectiveness of the CEX effect appears to be much greater near the peak of the geomagnetically-trapped proton density at  $L = 3.2$ . Fig. 6 shows the varied distance simulation results for the  $L = 3.2$  case, similar to Fig. 4 for the 1000 km case. The  $\Delta v$  predicted by the model is a full six orders of magnitude greater than for the 1000 km altitude simulation. Likewise, Fig. 7 shows the same difference in effectiveness when compared to its 1000 km analog, Fig. 5. The relationships between the varied parameters and the  $\Delta v$  are still valid, but the higher proton radiation density leads to more significant results. Even so, from a debris remediation standpoint the  $L = 3.2$  case will be less effective than the 1000 km case because the debris field is much more sparse at 14,031 km than it is at 1000 km.

Simulation of a single object through simplified density fields using the expanding gas cloud code reveals the numerical accuracy of the code. Because the density is a function of both time and space, an analytical solution to Eq. (18) is impractical. Instead, analytically solvable density fields which are a function of time or space only verify the time-varying and space-varying parts of the code independently. The first density field takes the form of a simple exponential in time given as:

$$\rho(t) = e^{-t} \quad (19)$$

Combining Eqs. (19) and (18), and solving for the final time in the simulation volume yields:

$$t_f = \ln \left( \frac{\exp \left[ \frac{(x(t_f) - x_0)(\frac{C_{DA}}{2m} v_0 + 1)}{v_0} \right] + \frac{C_{DA}}{2m} v_0}{\frac{C_{DA}}{2m} v_0 + 1} \right) \quad (20)$$

where  $v_0$  is the initial velocity and  $x_0$  is the initial position. The second density field takes the form of a simple inverse-square relationship with radius:

$$\rho(r) = \frac{1}{r^2} \quad (21)$$

which, combined with Eq. (18) yields a solution for the final velocity:

$$v(t_f) = v_0 \exp \left\{ \frac{\frac{C_{DA}}{2m}}{\sqrt{y^2 + z^2}} \left[ \tan^{-1} \frac{x_0}{\sqrt{y^2 + z^2}} - \tan^{-1} \frac{x(t_f)}{\sqrt{y^2 + z^2}} \right] \right\} \quad (22)$$

where  $y$  and  $z$  are the coordinates for the object off of the direction of motion. Using numerous initial conditions and object properties the difference between the numerical and analytical solutions is consistently under 1%.

Results are averaged over 1000 independent and random simulation runs for each test case. Table 2 contains the average results from each test case. The second column presents the sum of the impulse imparted to each debris object which passed through the gas cloud. In other words, the second column represents the total impulse imparted to the entire debris field from the gas cloud. This value is around 83 N-s for gas clouds release from orbits which are non-retrograde. For comparison, the maximum impulse available from proton collisions at 1000 km is  $5.85 \times 10^{-4}$  N-s. Even if every neutralized proton struck a piece of debris in the environment the total impulse imparted to the debris field would still be six orders of magnitude smaller than the impulse imparted by drag. This six orders of magnitude difference in impulse imparted from drag compared to impulse available from proton collisions establishes drag as the dominant effect present in this approach. The impulse imparted from the retrograde orbiting gas cloud exceeds that of the non-retrograde cases by a

Table 2

Results from the drag effect simulation for each test case, including the impulse imparted to the debris field from drag and the average percentage of debris objects which lose all relative velocity with the gas cloud and enter its orbit.

Case	Average total impulse imparted to nearby debris field (N-s)	Average percentage of objects which attain cloud's orbit
Case 1: 1000 km altitude circular orbit, 0° inclination	81.885	94.15
Case 2: 1000 km apogee, 200 km perigee orbit, 0° inclination	82.900	94.08
Case 3: 1000 km apogee, 200 km perigee orbit, 180° inclination	1787	89.49

factor of 20. This result arises from a higher average relative velocity between the debris and the gas cloud and establishes a retrograde deployment of gas as a more effective means of transferring momentum away from the debris field.

The data in the right column of Table 2 are the average percentages of debris objects which attain the gas cloud's deployment orbit. Debris with high  $A/m$  ratio and/or that pass through the high density region of the gas cloud shortly after release experience so much drag that they reach zero relative velocity within the gas cloud. When this occurs, this debris has the same position and velocity as the gas cloud and consequently has the same orbit. Between 89% and 94% of the simulated debris objects are "swept" into the gas cloud deployment orbit. This percentage decreases as the relative velocity between the debris objects and the gas cloud increases.

## 5. Conclusion

The concept of orbit perturbation via CEX reactions with near-Earth proton radiation requires a gas cloud, which produces a secondary effect of inducing drag on nearby debris. While proton collisions on debris occur, they are negligible compared to the effect of induced drag from the gas cloud. The near-Earth proton radiation environment has a number density which is orders of magnitude too low to allow for significant perturbations to be made from CEX collisions. The technique could be of use in regions of space with a much more populous radiation environment. However; the neutral gas cloud release idea has potential applications in the near-Earth environment for orbit perturbation of multiple objects simultaneously, especially in space debris remediation. This work has demonstrated that the drag effect from an expanding neutral gas cloud can force a majority of intersecting debris into the orbit of the gas cloud without adding to the debris population or affecting operational assets.

## References

- Anselmo, L., Pardini, C. Long-term dynamical evolution of high area-to-mass ratio debris released into high earth orbits. *Acta Astronaut.* 67, 204–216, 2009.
- Atchison, J.A., Peck, M.A. Length scaling in spacecraft dynamics. *J. Guid. Cont. Dyn.* 34, 231–245, 2011.
- Baker, D.N., Kanekal, S.G., Li, X., et al. An extreme distortion of the Van Allen belt arising from the Halloween solar storm in 2003. *Nature* 432, 878, 2004.
- Baumjohann, W., Treumann, R.A. *Basic Space Plasma Physics*. World Scientific, London, pp. 32–33, 1997.
- Belk, C.A., Robinson, J.H., Alexander, M.B., et al. Meteoroids and orbital debris: effects on spacecraft. NASA, Marshall Space Flight Center, 1997.
- Bernhard, R.P., Christiansen, E.L., Hyde, J., et al. Hypervelocity impact damage into space shuttle surfaces. *Int. J. Impact Eng.* 17, 57–68, 1995.
- Carslaw, H.S., Jaeger, J.C. *Conduction of Heat in Solids*. Oxford Univ. Press, Oxford, pp. 256–257, 1959.
- Christiansen, E.L., Kerr, J.H. Ballistic limit equations for spacecraft shielding. *Int. J. Impact Eng.* 26, 93–104, 2001.
- Colombo, C., Lucking, C., McInnes, C.R. Orbit evolution, maintenance and disposal of SpaceChip swarms through electro-chromic control. *Acta Astronaut.* 82, 25–37, 2013.
- Cook, G.E. Satellite drag coefficients. *Planet. Space Sci.* 13, 929–946, 1965.
- Gibbons, J.H. Interagency report on orbital debris. NS&T Council, Washington, D.C., 1995.
- Griffiths, D.J. *Introduction to Quantum Mechanics*. Pearson Prentice Hall, Upper Saddle River, pp. 415–416, 2005.
- Hedin, A.E. The atmospheric model in the region 90–2000 km. *Adv. Space Res.* 8, 9–25, 1988.
- Kawaguchi, J., Mimasu, Y., Mori, O., et al. IKAROS - ready for lift-off as the world's first solar sail demonstration in interplanetary space. In: 60th Int. Astro. Cong., Daejon, South Korea, 2009.
- Liou, J.C., Matney, M.J., Anz-Meador, P.D., et al. The new NASA orbital debris engineering model ORDEM2000. NASA, 2002.
- Liou, J.C., Johnson, N.L., Hill, N.M. Controlling the growth of future LEO debris populations with active debris removal. *Acta Astronaut.* 66, 648–653, 2010.
- Mapleton, R.A. Electron capture from atomic nitrogen by protons. *Phys. Rev.* 145, 25–26, 1965.
- McCormack, P.D. Radiation dose and shielding for the space station. *Acta Astronaut.* 17, 231–241, 1988.
- McIlwain, C.E. Coordinates for mapping the distribution of magnetically trapped particles. *J. Geophys. Res.* 66, 3681–3691, 1961.
- Mehrholz, D., Leushacke, L., Flury, W., et al. Detecting, tracking and imaging space debris. *ESA Bull.* 109, 128–134, 2002.
- Molmud, P. Expansion of a rarefied gas cloud into a vacuum. *Phys. Fluids* 3, 362–366, 1960.
- Pardini, C., Anselmo, L. Physical properties and long-term evolution of the debris clouds produced by two catastrophic collisions in Earth orbit. *Adv. Space Res.* 48, 557–569, 2011.
- Patera, R.P., Ailor, W.H. The realities of reentry disposal. In: AAS/AIAA Space Flight Mech. Meet., Monterey, CA, pp. 1059–1071, 1998.
- Sawyer, D.M., Vette, J.I. AP-8 trapped proton environment for solar maximum and solar minimum. NASA, 1976.
- Stassinopoulos, E.G., Raymond, J.P. The space radiation environment for electronics. *Proc. IEEE* 76, 1423–1442, 1988.
- Vallado, D.A., Finkelman, D.A. Critical assessment of satellite drag and atmospheric density modeling. In: AIAA/AAS Astrodyn. Spec. Conf., Honolulu, Hawaii, 2008.
- Van Allen, J.A., Ludwig, G.H., Ray, E.C., et al. The observation of high intensity radiation by satellites 1958 alpha and gamma. *Ann. Int. Geophys.* Yr. 12, 671–682, 1961.
- Vernov, S.N., Gorchakov, E.V., Shavrin, P.I., et al. Radiation Belts in the region of the south-Atlantic magnetic anomaly. *Space Sci. Rev.* 7, 490–533, 1967.
- Welsh, L.M., Berkner, K.H., Kaplan, S.N., et al. Cross sections for electron capture by fast protons in H<sub>2</sub>, He, N<sub>2</sub>, and Ar. *Phys. Rev.* 158, 85–92, 1967.
- Zhou, Y.L., Ma, S.Y., Luhr, H., et al. An empirical relation to correct storm-time thermospheric mass density modeled by NRLMSISE-00 with CHAMP satellite air drag data. *Adv. Space Res.* 43, 819–828, 2009.